Journal of Materials Chemistry A

PAPER

View Article Online

Cite this: DOI: 10.1039/c7ta03093b

A freestanding cellulose nanofibril–reduced graphene oxide–molybdenum oxynitride aerogel film electrode for all-solid-state supercapacitors with ultrahigh energy density†

Qifeng Zheng,[ab] Alexander Kvit,[c] Zhiyong Cai,[d] Zhenqiang Ma[e] and Shaoqin Gong*[abf]

A free-standing, lightweight, highly porous, and highly flexible cellulose nanofibril (CNF)–reduced graphene oxide (RGO)–molybdenum oxynitride (MoO_xN_y) aerogel film electrode was synthesized by freeze-drying a CNF/GO/MoO_3 aqueous dispersion followed by subsequent *in situ* hydrazine reduction. Due to the partial reduction and nitrogen doping of the MoO_3 nanobelts and the highly open and continuous porous structure, the free-standing CNF/RGO/MoO_xN_y aerogel film electrode delivered an outstanding specific capacitance of 680 F g^{-1} in an aqueous electrolyte and 518 F g^{-1} in an ionic liquid electrolyte in a three-electrode configuration at a current density of 1.0 A g^{-1}. Furthermore, highly flexible and all-solid-state supercapacitors using CNF/RGO/MoO_xN_y as electrodes and either a hydrogel or ionogel as the electrolyte were fabricated and both types of supercapacitors demonstrated high specific capacitance and excellent long-term cycling stability. Remarkably, the solid-state supercapacitor devices fabricated using an ionogel electrolyte demonstrated an energy density of 114 W h kg^{-1} (corresponding to a volumetric energy density of 18.8 W h L^{-1}), which is among the highest values achieved for any type of solid-state supercapacitor and is even comparable to the energy densities of Li-ion batteries. Therefore, this study provides a simple and cost-efficient method for fabricating flexible energy storage devices with excellent electrochemical performance.

Received 9th April 2017
Accepted 17th May 2017

DOI: 10.1039/c7ta03093b

rsc.li/materials-a

1. Introduction

Due to the rapidly growing market for portable electronic devices and hybrid vehicles, energy conversion and storage devices with high energy and power densities are in ever-increasing demand.[1–3] Supercapacitors, also known as electrochemical capacitors, have attracted a great deal of attention due to their higher power densities (1–2 orders of magnitude higher), longer life cycles (1–3 orders of magnitude longer), and fast charge–discharge capabilities when compared to conventional energy storage devices such as Li-ion batteries.[4–6] Different from batteries, which are generally limited by slow reactions,[5] supercapacitors store charges *via* highly reversible electric double-layer ion adsorption and/or fast faradaic redox reactions,[4] which makes them ideal energy storage candidates for portable electronic devices and hybrid vehicles where rapid energy capture and delivery are needed. Nevertheless, supercapacitors often suffer from lower energy densities (typically less than 10 W h kg^{-1}) when compared with Li-ion batteries (>50 W h kg^{-1}).[6] Therefore, improving the energy density without compromising the power density and cycling stability for supercapacitors still remains an ongoing challenge.[7] According to the energy density equation $E = 1/2CV^2$,[7,8] the energy density of supercapacitors can be dramatically improved by increasing the capacitance (C) and/or operating voltage (V).

Currently, carbon nanomaterials (*e.g.*, graphene and carbon nanotubes) have been extensively explored as electrode materials for high-performance supercapacitors owing to their high specific surface area, high electrical conductivity, excellent chemical stability, and good environmental compatibility.[9,10] Porous graphene materials with large specific surface areas and optimal pore sizes generally have a higher capability for charge accumulation at the electrode/electrolyte interface, thereby yielding higher-performance supercapacitors.[11,12] Thus, various methods have been investigated to develop porous graphene

[a]Department of Material Science and Engineering, University of Wisconsin–Madison, WI 53706, USA. E-mail: shaoqingong@wisc.edu; Tel: +1 6083164311
[b]Wisconsin Institute for Discovery, University of Wisconsin–Madison, WI 53715, USA
[c]Materials Science Center, University of Wisconsin–Madison, Madison, WI 53706, USA
[d]Forest Product Laboratory, USDA, Madison, WI 53726, USA
[e]Department of Electrical Engineering, University of Wisconsin–Madison, WI 53706, USA
[f]Department of Biomedical Engineering, University of Wisconsin–Madison, WI 53706, USA

† Electronic supplementary information (ESI) available. See DOI: 10.1039/c7ta03093b

materials, including chemical vapor deposition (CVD) growth of 3D graphene on porous metal foam templates,[13,14] high-temperature treatment of carbon-rich polymer precursors[15] (*e.g.*, resorcinol and formaldehyde), and freeze-drying of a graphene oxide (GO) suspension followed by reduction.[16–18] Among the various methods, freeze-drying is considered to be the most inexpensive and environmentally friendly approach.[19,20]

Introducing pseudocapacitive materials such as metal oxides (*e.g.*, MnO_2 and RuO_2) and conductive polymers into the electrodes, that are capable of fast and reversible redox reactions at the electrode surface, will result in much higher capacitances compared to carbon-based materials alone.[4] Orthorhombic molybdenum trioxide (MoO_3), which has an anisotropic-layered structure as well as a high theoretical specific capacity and energy density, has been recognized as a promising electrode material for electrochemical energy storage systems such as Li-ion batteries.[21,22] However, the low electrical conductivity and inferior chemical stability of MoO_3 have severely hindered its application in high-performance energy storage systems.[21,23] Various approaches have been investigated to increase the conductivity and electrochemical stability of MoO_3 such as nitrogen doping and introducing oxygen vacancies.[21,24,25] For instance, Wang *et al.*[21] reported that hydrogen intercalation and nitrogen substitution by ammonolysis of MoO_3 at 280 C for 10 h led to the formation of the compound $H_xMo(O,N)_3$, which subsequently led to higher capacitance and better cycling stability in comparison with regular MoO_3 when used as the cathode material for Li-ion batteries. Nevertheless, the reported approaches for nitrogen doping only occurred at high temperature (*i.e.*, typically more than 280 C), and thus there is still a need to develop a novel method to perform nitrogen doping at a moderate temperature and thereby not to reduce the metal oxide excessively.

Aside from strategies to enhance the capacitance of supercapacitors, increasing the operating voltage of supercapacitors is an alternative, yet very effective approach to further increase the energy density of supercapacitors since the energy density is proportional to the square of the operating voltage. The operating voltage of supercapacitors is strongly affected by the type of electrolyte employed. Aqueous electrolytes are the most commonly used owing to their low cost, high ionic concentration, and low resistance. Nevertheless, a large disadvantage of such systems is their small operating voltage ranges (*i.e.*, <1.2 V).[4] Ionic liquids (ILs), which are known as room-temperature salts, exhibit a number of unique properties desirable for electrolytes including excellent electrochemical and thermal stability, as well as low vapor pressure.[26,27] Compared to aqueous electrolytes, ionic liquid electrolytes can provide a voltage window as high as 6 V, which will greatly increase the power and energy densities of supercapacitors.[26,28]

In this work, we have successfully prepared cellulose nanofibril (CNF)–graphene oxide (GO)–molybdenum trioxide (MoO_3) hybrid aerogels with a high mass loading of MoO_3 (*i.e.*, 30 wt%) *via* an environmentally friendly freeze-drying process.[19,20] Upon hydrazine vapor treatment of the compressed CNF/GO/MoO_3 aerogel film, the partial reduction and nitrogen doping of the MoO_3 nanobelts occurred simultaneously with the reduction of GO to reduced graphene oxide (RGO), resulting in a free-standing, lightweight, highly porous, and highly flexible CNF–RGO–molybdenum oxynitride (MoO_xN_y) aerogel film electrode. Significantly, the resulting free-standing CNF/RGO/MoO_xN_y aerogel film electrode delivered an outstanding specific capacitance of 680 F g ^{1} in an aqueous electrolyte and 518 F g ^{1} in an ionic liquid electrolyte in a three-electrode configuration at a current density of 1.0 A g ^{1}. Furthermore, highly flexible and all-solid-state supercapacitors using CNF/RGO/MoO_xN_y as electrodes and poly(vinyl alcohol) (PVA)–H_2SO_4 hydrogel or poly(vinylidene fluoride) (PVDF)–poloxamer 407 (P407)–1-butyl-1-methylpyrrolidinium bis(trifluoromethylsulfonyl) imide ([BMPY][NTf_2]) ionogel as solid-state electrolytes were fabricated. These supercapacitors exhibited high specific capacitances and high energy densities while maintaining high power densities and excellent long-term cycling stabilities. Considering their excellent electrochemical performance, ease of large-scale manufacturing, and environmental friendliness, this study provides a promising approach for fabricating porous flexible electrodes for assembling lightweight and low-cost energy storage devices.

2. Experimental section

2.1. Preparation of CNF/RGO/MoO_xN_y aerogel film electrodes

GO powder (30 mg) and MoO_3 nanobelts (NBs, 30 mg) were first added to deionized water (10 mL). Next, the mixture was sonicated (UP400S, Hielscher USA) at 50% amplitude using a 3 mm probe in an ice-bath for 30 min. CNF solution (4.7 g, 0.85 wt%) was then added to the above GO/MoO_3 dispersion under continuous magnetic stirring at room temperature to yield a homogeneous mixture. The weight percentages of GO, MoO_3, and CNFs were 30%, 30%, and 40%, respectively. After being transferred into an aluminum pan, the CNF/GO/MoO_3 aerogel was obtained by a freeze-drying process as reported previously by our group.[19,20] The CNF/GO/MoO_3 aerogels were then compressed into aerogel films under a pressure of 1.0 MPa. At the final stage, the CNF/GO/MoO_3 aerogel films and a small glass vial containing hydrazine monohydrate (1.0 mL) were placed in a vacuum oven with calcium oxide (CaO) (100 g) at the bottom of the oven. The CNF/GO/MoO_3 aerogel films were converted into CNF/RGO/MoO_xN_y aerogel films after they were heated in the vacuum oven at 120 C for 12 h at 85 kPa below atmospheric pressure. For comparison, CNF (40 wt%)/RGO(60 wt%) aerogel films were also prepared using the same procedure.

2.2. Preparation of the PVA–H_2SO_4 hydrogel electrolyte

Following the typical process,[29] H_2SO_4 (2 mL, 98 wt%) was first added to deionized water (20 mL). Then PVA powder (2.0 g) was added to the solution, and the resulting mixture was subsequently heated to 80 C under vigorous stirring for 10 h.

2.3. Preparation of the PVDF–P407–[BMPY][NTf_2] ionogel electrolyte

Following the typical process, PVDF powder (80 mg) was first dissolved in DMF (4 mL) at 80 C under vigorous stirring for 6 h.

Poloxamer 407 triblock copolymer (80 mg) and 1-butyl-1-methylpyrrolidinium bis(trifluoromethylsulfonyl)imide ([BMPY][NTf_2], 1.84 g) were dissolved in acetonitrile (5.0 mL) and then the mixture was added to the above PVDF DMF solution. The resulting mixture was continuously stirred for another 6 h at 80 C. Afterward, the acetonitrile was removed at 100 C for 4 h using a vacuum line. The weight percentages of PVDF, P407, and [BMPY][NTf_2] were 4%, 4%, and 92%, respectively.

2.4. Preparation of flexible all-solid-state supercapacitors

The CNF/RGO/MoO_xN_y aerogel film was cut into pieces (1 cm 2.4 cm in area, 150 μm in thickness). Aluminum foil was affixed to one side of the aerogel film using silver paste, which acted as a current collector and also ensured good electrical contact of the electrode with the electrochemical testing machine. Thereafter, the hot (80 C) gel electrolyte (*i.e.*, PVA–H_2SO_4 hydrogel electrolyte or PVDF–P407–[BMPY][NTf_2] ionogel electrolyte, 200 μL electrolyte per cm^2 of the electrode) was slowly poured onto the aerogel film. Following a vacuum-assisted liquid filling method, the gel electrolyte completely infiltrated through the porous structure of the aerogel film. Next, the electrode coated with a thin layer of gel electrolyte was left in a fume hood at room temperature for about 12 h to vaporize the solvent (*i.e.*, water or DMF). Finally, two pieces of the resulting aerogel film covered by the electrolyte were then assembled face-to-face into an all-solid-state flexible supercapacitor under a pressure of 0.2 MPa for 10 min, which allowed the gel electrolyte layer on each electrode to merge into one thin separator. For comparison, CNF/RGO aerogel films were also used to prepare supercapacitors *via* the same procedure.

2.5. Characterization and electrical measurements

All tests described in this manuscript were done at least in triplicate, and the most representative curves and the average results were reported. The densities of the aerogels were calculated by measuring the mass and volume of the aerogels. The microstructures of the aerogels were studied using a scanning electron microscope (SEM, LEO GEMINI 1530) and a transmission electron microscope (TEM, TF-30). Energy-dispersive X-ray spectroscopy (EDS) of the MoO_3 NBs after hydrazine vapor reduction was carried out using an FEI Titan TEM with a corrector working at 200 kV. The SEM samples were treated using gold sputtering. TEM samples were prepared by dissolving the CNF/RGO/MoO_xN_y aerogel film in ethanol under sonication to obtain a uniform dispersion, which was then added dropwise onto the surface of copper TEM grids. The aerogel samples were compressed using an Instron (Model 5967) equipped with a 30 kN load. Thermal stability measurements were carried out using a thermogravimetric analyzer (TGA, Q50 TA Instruments, USA) from 30 to 800 C at a 10 C min^{-1} heating rate under N_2 protection. Elemental analysis was performed on a K-Alpha™+ X-ray Photoelectron Spectrometer (XPS, Thermo Scientific, USA) with focused monochromatic AlKα X-rays ($h\nu$ = 1286.6 eV). X-ray diffraction (XRD) patterns were obtained on a D8-Discovery diffractometer (Bruker, USA) with Cu-Kα radiation at a scan rate of 5 min^{-1}. Raman spectra were collected on a DXR™ Raman spectrophotometer (Thermo Scientific, USA) equipped with a 633 nm laser source. The Brunauer–Emmett–Teller (BET) specific surface area was determined by N_2 physisorption using a Gemini analyzer (Micromeritics, USA). The electrochemical performances of the aerogel film electrodes were evaluated in both a three-electrode system and a two-electrode solid-state supercapacitor system using cyclic voltammetry (CV) and galvanostatic charge–discharge measurements. All electrochemical tests were carried out on a versaSTAT-3 electrochemical workstation (Princeton Applied Research, USA). For the three-electrode system, a piece of 0.24 cm^2 as-prepared aerogel film was used directly as the working electrode. For the aqueous-based three-electrode system, an Ag/AgCl electrode, platinum wire, and 1 M H_2SO_4 aqueous solution were used as the reference electrode, counter electrode, and electrolyte, respectively. For the ionic liquid (IL)-based three-electrode system, a silver wire, platinum wire, and 50 vol% [BMPY][NTf_2] in acetonitrile solution were used as the quasi-reference electrode, counter electrode, and electrolyte, respectively. Electrochemical impedance spectroscopy (EIS) was performed at open circuit potential with an amplitude of 10 mV over a frequency range of 0.01 Hz to 100 kHz.

3. Results and discussion

3.1. Preparation and characterization of CNF/RGO/MoO_xN_y aerogel film electrodes

Ultralong MoO_3 nanobelts (NBs) were prepared using a modified hydrothermal method as reported previously at 220 C for 168 h.[30] As shown in Fig. S1(a) and (b),† the MoO_3 NBs exhibited a very uniform morphology with lengths of 100–200 μm, widths of 300–500 nm, and thicknesses of 50–80 nm. The ultralong MoO_3 NBs will be beneficial for forming free-standing and flexible films.[30] X-ray diffraction (XRD) patterns demonstrated that as-synthesized MoO_3 NBs had an orthorhombic structure (Fig. S2†).[21,30] Graphene oxide (GO) was prepared from purified natural graphite powder using an improved Hummer's method reported by Marcano.[31] Since GO has a large amount of oxygen-containing groups, it can act as a surfactant to facilitate the dispersion of the MoO_3 NBs in aqueous solutions.[29,32] CNFs derived from cellulose often exhibit high aspect ratios, high surface areas, superior mechanical properties, and excellent flexibility,[33,34] which can be integrated with GO and/or MoO_3 easily to achieve flexible, free-standing, and binder-free electrodes.

As shown in Scheme 1, the CNF, GO, and MoO_3 were first mixed together to obtain a uniform CNF/GO/MoO_3 dispersion *via* sonication. By freeze-drying the CNF/GO/MoO_3 aqueous dispersion, an ultra-light CNF/GO/MoO_3 aerogel (about 6 mg mL^{-1}, Fig. S3†) was obtained, which exhibited a highly interconnected and porous cellular structure with pore sizes ranging from 5 to 10 μm (Fig. S4†). A CNF/GO/MoO_3 aerogel film with a uniform thickness of about 150 μm was obtained by compressing the aerogel at 1 MPa. For comparison purposes, a CNF/GO aerogel film (*i.e.*, without MoO_3 NBs) was prepared using a similar procedure. The CNF/GO and CNF/GO/MoO_3 aerogel films were then subjected to the hydrazine vapor reduction at

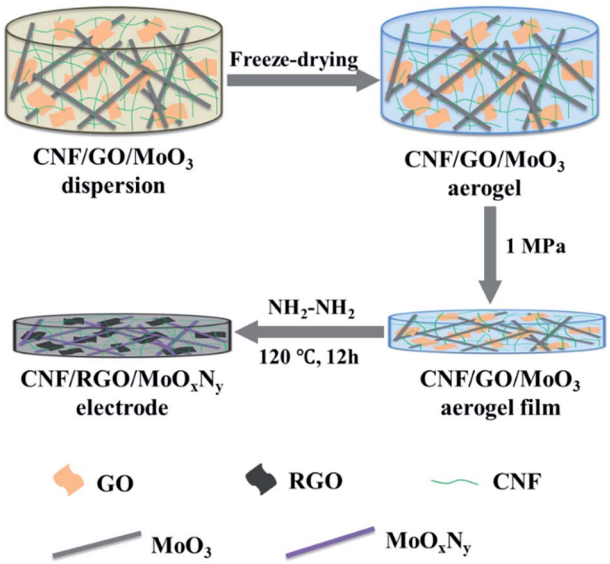

Scheme 1 The fabrication process of a porous CNF/RGO/MoO_xN_y aerogel film electrode.

120 C for 12 h. A number of techniques including XRD, high resolution transmission electron microscopy (HR-TEM), energy-dispersive X-ray spectroscopy (EDS), Raman spectroscopy, X-ray photoelectron spectroscopy (XPS) and scanning electron microscopy (SEM) were used to study the structure and morphology change during the hydrazine reduction process.

As shown in Fig. S5(a),† the X-ray diffraction (XRD) pattern of the CNF/GO aerogel film exhibited a strong diffraction peak at $2\theta = 10.9$, corresponding to the (002) lattice planes of the GO nanosheets.[29] After the CNF/GO aerogel film was treated with hydrazine vapor at 120 C for 12 h, the diffraction peak at 10.9 vanished, indicating a complete reduction of GO.[29,35] Fig. 1(a) shows the XRD patterns of the CNF/GO/MoO_3 aerogel films before and after hydrazine vapor reduction. The intensities of diffraction patterns of the α-MoO_3 decreased significantly after 12 h hydrazine vapor reduction, while several new diffraction peaks at $2\theta = 11.0$, 22.5 , 24.3 and 38.5 appeared. This phenomenon has been previously observed, suggesting that α-MoO_3 was mainly converted to MoO_xN_y (defined as phase X by Li *et al.*, an unresolved crystalline phase).[36,37] Thus, the XRD analyses indicate that the CNF/GO and CNF/GO/MoO_3 aerogel films were converted to CNF/RGO and CNF/RGO/MoO_xN_y aerogel films, respectively, after hydrazine vapor reduction.

Fig. 1(b) and (c) show the TEM images of the MoO_xN_y NBs in the CNF/RGO/MoO_xN_y aerogel film. As shown in Fig. 1(c), the high resolution TEM (HR-TEM) image and selected area electron diffraction (SAED) pattern suggest that the MoO_xN_y NBs (*i.e.*, MoO_3 NBs after hydrazine reduction) still exhibited an orthorhombic crystalline structure with an interplanar spacing of 0.41 and 0.45 nm, respectively, along the two perpendicular directions. However, these values were slightly different from the *d*-space of the orthorhombic MoO_3 NBs (*i.e.*, 0.37 and 0.40 nm),[30] indicating that the orthorhombic MoO_3 NBs may be converted to a new crystalline structure (phase X) during the hydrazine reduction process. Fig. S6† shows the TEM energy-dispersive X-ray (EDS) spectrum of MoO_xN_y NBs, which showed characteristic peaks for molybdenum, oxygen, carbon, and nitrogen. The relative nitrogen atomic percentage by element was about 2.1%. The presence of a nitrogen peak confirmed that nitrogen doping occurred during the hydrazine reduction process. Namely, the MoO_3 NBs were converted to MoO_xN_y NBs (eqn (1)), which is consistent with our XRD analysis (Fig. 1(a)).

$$MoO_3 + NH_2\text{–}NH_2 \rightarrow MoO_xN_y + (3\quad x)H_2O + (x\quad 1)H_2 + (1\quad 0.5y)N_2 \quad (1)$$

Fig. S7† shows the Raman spectra of the CNF/GO, CNF/RGO, CNF/GO/MoO_3, and CNF/RGO/MoO_xN_y aerogel films. Two distinct peaks at 1338 and 1587 cm ^{1}, corresponding to the well-documented graphene D and G bands, respectively, were observed for all samples. The intensity ratio of the D and G bands (*i.e.*, I_D/I_G) for CNF/RGO was 1.35, which was higher than that of CNF/GO (*i.e.*, 1.06), thus indicating that the GO in the CNF/GO aerogel film was successfully reduced to RGO.[38] Specifically, the increase of the I_D/I_G value had previously been attributed to the creation of new sp^2 graphitic domains in RGO that were smaller in size than the ones present in the GO nanosheets before reduction, but more numerous in number.[38] It is worth noting that the I_D/I_G value for CNF/GO/MoO_3 (*i.e.*, 1.18) was higher than that of CNF/GO (*i.e.*, 1.06), which may be attributable to the addition of MoO_3 that enhanced the defect structures of the GO nanosheets. Furthermore, the I_D/I_G value for the CNF/RGO/MoO_xN_y aerogel film increased to 1.45, thus confirming that the GO in the CNF/GO/MoO_3 aerogel film was converted into RGO. In addition, thermogravimetric (TGA) and differential thermogravimetric (DTG) analyses also suggested that GO was successfully reduced to RGO in both the CNF/GO and CNF/GO/MoO_3 aerogel films during the hydrazine vapor reduction process (Fig. S8†).

X-ray photoelectron spectroscopy (XPS) was employed to further confirm the successful reduction of GO in the CNF/GO and CNF/GO/MoO_3 aerogel films. In order to investigate the effect of reduction time on the reduction and nitridation of MoO_3 NBs, the CNF/GO/MoO_3 aerogel films were subjected to hydrazine vapor at 120 C for 6 or 12 h. As shown in Fig. S9(a),† the intensity ratio of C 1s to O 1s gradually increased when the CNF/GO/MoO_3 aerogel film was subjected to 6 h and 12 h of hydrazine reduction. Fig. 1(d–f) show the high-resolution C 1s XPS spectra of the CNF/GO/MoO_3 aerogel film and the CNF/GO/MoO_3 aerogel film after either 6 or 12 h of hydrazine reduction. The peak intensity of C=C/C–C of the CNF/GO/MoO_3 aerogel film increased significantly with increased reduction time, suggesting that GO was effectively reduced during the hydrazine vapor reduction process. Nevertheless, a relatively large amount of oxygen-containing functional groups were still present after 12 h of reduction. These oxygen-containing functional groups were mainly attributed to the CNFs and MoO_3 NBs present in the aerogel films. Similar results have also been observed for CNF/GO aerogel films after being subjected to hydrazine vapor reduction (Fig. S10†).

Fig. 1(g–i) show the high-resolution Mo 3d XPS spectra of the CNF/GO/MoO_3, and the CNF/GO/MoO_3 aerogel film after either

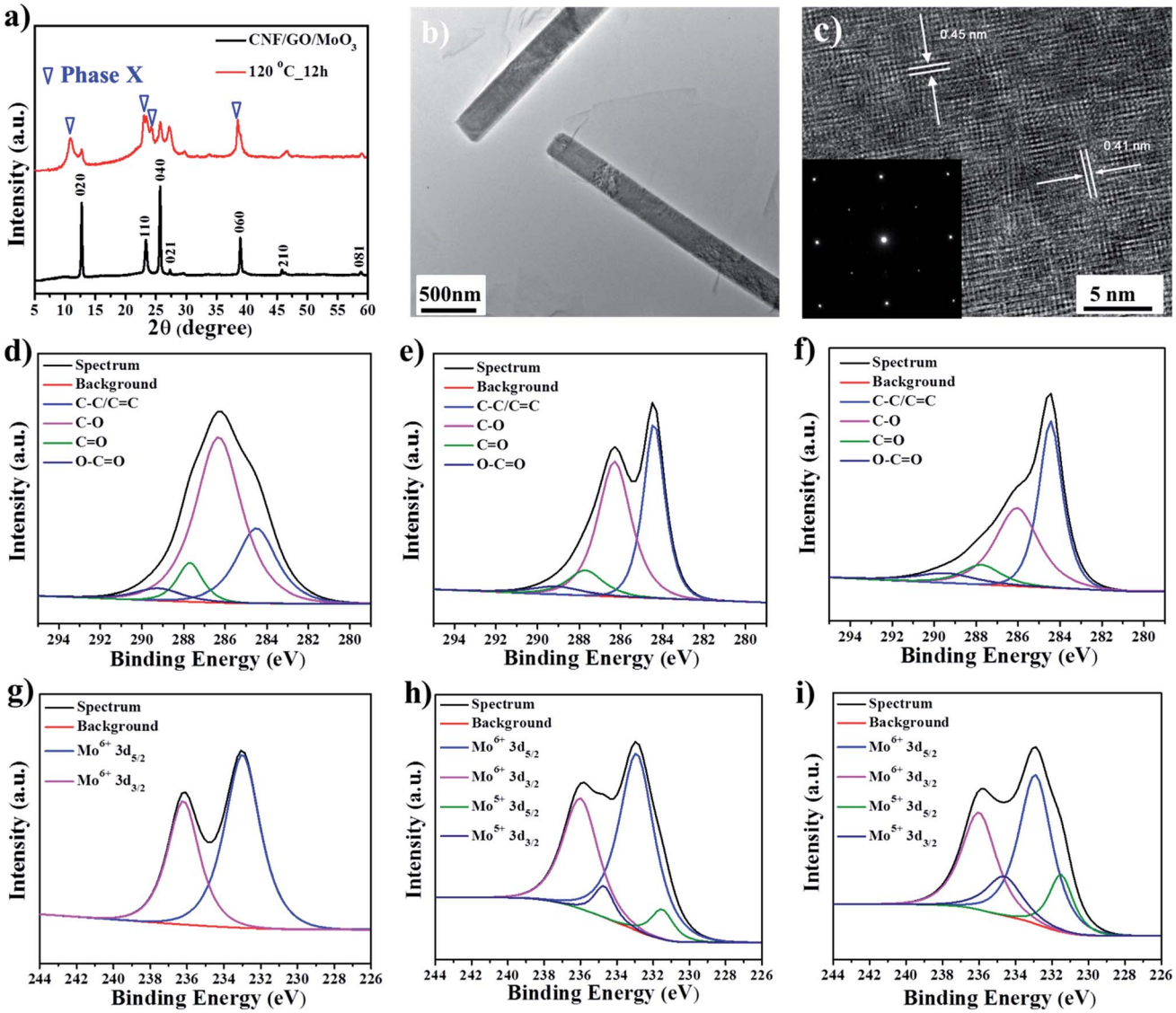

Fig. 1 (a) XRD patterns of the CNF/GO/MoO_3 and CNF/RGO/MoO_xN_y aerogel films. (b) TEM image, and (c) HR-TEM image of the MoO_xN_y NBs in the CNF/RGO/MoO_xN_y aerogel film. The inset in (c) is a selected area electron diffraction (SAED) pattern. High-resolution C 1s XPS spectra of the (d) pristine CNF/GO/MoO_3 aerogel film, and CNF/GO/MoO_3 aerogel film after either (e) 6 h, or (f) 12 h hydrazine reduction. High-resolution Mo 3d XPS spectra of the (g) pristine CNF/GO/MoO_3 aerogel film, and CNF/GO/MoO_3 aerogel film after either (h) 6 h, or (i) 12 h hydrazine reduction.

6 or 12 h of hydrazine reduction. As shown in Fig. 1(g), two strong peaks at 232.9 eV and 236.0 eV can be attributed to Mo^{6+} $3d_{5/2}$ and Mo^{6+} $3d_{3/2}$, respectively, which are the characteristic peaks of MoO_3.[21,24] After the CNF/GO/MoO_3 aerogel film was subjected to hydrazine reduction for 6 h, two new peaks at 231.5 eV and 234.8 eV were found and could be assigned to Mo^{5+} $3d_{5/2}$ and Mo^{5+} $3d_{3/2}$ (Fig. 1(h)), respectively, indicating that the partial reduction of Mo^{6+} occurred during the hydrazine reduction process.[24] As shown in Fig. 1(i), the peak intensities of Mo^{5+} $3d_{5/2}$ and Mo^{5+} $3d_{3/2}$ were further increased as the reduction time increased to 12 h.

As shown in Fig. 2(a and b), the highly porous microstructure of the CNF/GO/MoO_3 aerogel was largely preserved in the compressed CNF/GO/MoO_3 aerogel film. Fig. 2(c) and (d) show the SEM images of the bottom surface of a CNF/RGO/MoO_xN_y aerogel film, from which it can be seen that the porous microstructure of the CNF/GO/MoO_3 aerogel film was very well preserved during the hydrazine vapor reduction process. The MoO_3 NBs were distributed uniformly in the aerogel film both before and after reduction. Furthermore, well stacked layers were observed in the cross-sectional SEM images of the CNF/RGO/MoO_xN_y aerogel film (Fig. 2(e and f)). In addition, a highly porous and layered microstructure was also observed for the CNF/RGO aerogel film electrode (*i.e.*, without MoO_xN_y) (Fig. S11†). The CNF/RGO/MoO_xN_y and CNF/RGO aerogel film electrodes showed high BET surface areas of 186.3 and 169.2 m^2 g^{-1}, respectively. The highly porous and layered microstructure of the compressed aerogel film electrode can facilitate the penetration of electrolytes and thus greatly enhance the electrolyte ion transport and charge transfer, thereby leading to superior supercapacitor performance.

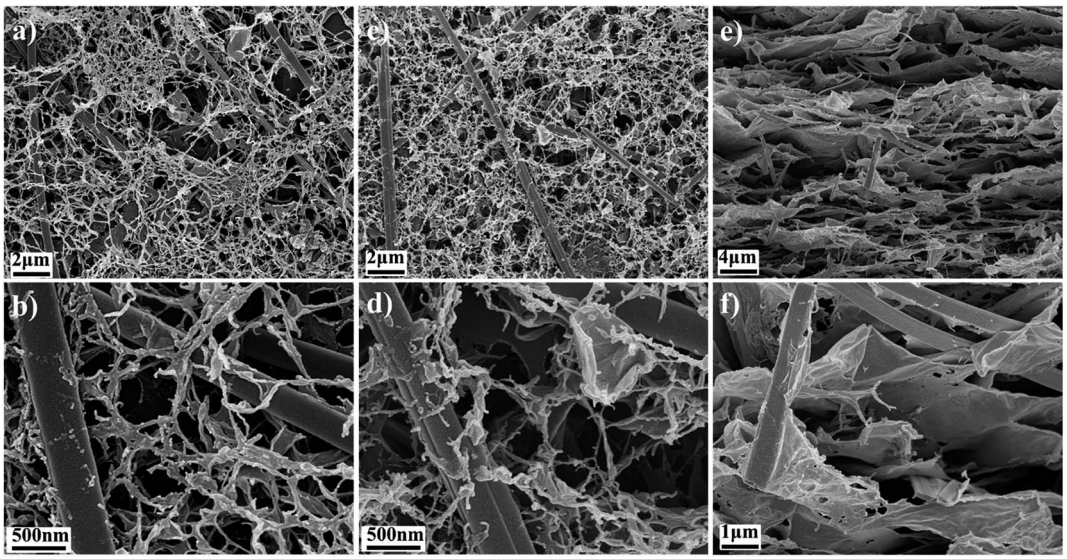

Fig. 2 SEM images of the CNF/GO/MoO_3 aerogel films: (a and b) the bottom surface of the aerogel film; SEM images of the CNF/RGO/MoO_xN_y aerogel films: (c and d) the bottom surface of the aerogel film, and (e and f) a cross-section of the aerogel film.

It is worth noting that the electrical conductivity of the pristine MoO_3 is very poor. However, after hydrazine reduction, the electrical conductivity of the CNF/RGO/MoO_xN_y aerogel film with 30 wt% MoO_3 (*i.e.*, 20.2 S m $^{-1}$) was similar to that of the CNF/RGO aerogel film (22.1 S m $^{-1}$). This may be attributed to the partial reduction and nitrogen doping of MoO_3 NBs, which were shown to greatly increase the electrical conductivity of the MoO_3 NBs.[21,24] Furthermore, previous studies have demonstrated that the partial reduction and nitrogen doping of MoO_3 NBs can not only increase their electrical conductivity, but also dramatically improve their electrochemical stability, thereby enhancing the supercapacitor performance when used as electrode materials.[21,24]

3.2. Electrochemical performance of the CNF/RGO/MoO_xN_y aerogel film electrodes in a three-electrode system

Free-standing and highly flexible CNF/RGO/MoO_xN_y aerogel films were used as electrodes for supercapacitors without the need for any binder or electroactive additives. In order to investigate the electrochemical performance of CNF/RGO/MoO_xN_y aerogel film electrodes, various electrochemical characterizations were carried out in 1.0 M H_2SO_4 aqueous electrolyte in a three-electrode system (Fig. 3). For comparison, a CNF/RGO aerogel film was also tested under the same conditions. Fig. 3(a) shows the cyclic voltammetry (CV) curves of the CNF/RGO and CNF/RGO/MoO_xN_y aerogel film electrodes at a scan rate of 10 mV s $^{-1}$. The CNF/RGO/MoO_xN_y aerogel film electrode exhibited a much higher capacitance than the CNF/RGO aerogel film, as demonstrated by a larger area enveloped in the CV curve. Specifically, some redox peaks, which may be ascribed to the redox reactions between various valences of Mo, appeared on the CV curve of the CNF/RGO/MoO_xN_y aerogel film electrode.[25,39] As shown in Fig. 3(b), the CV curve of the CNF/RGO/MoO_xN_y aerogel film electrode exhibited a similar feature with an increasing enveloped area as the scan rate increased from 5 to 100 mV s $^{-1}$, thus implying fast charge transfer. Fig. 3(c) shows the galvanostatic charge–discharge curves of the CNF/RGO and CNF/RGO/MoO_xN_y aerogel film electrodes at a current density of 2 A g $^{-1}$. The CNF/RGO aerogel film electrode exhibited a relatively symmetrical triangular shape suggesting ideal electric double-layer capacitive behavior, while the CNF/RGO/MoO_xN_y aerogel film electrodes exhibited distinct pseudocapacitive behavior,[4,25] which is consistent with the CV measurements. Fig. 3(d) and S12(b)† show the galvanostatic charge–discharge curves of the CNF/RGO and CNF/RGO/MoO_xN_y aerogel film electrodes at various current densities. The specific capacitances at various current densities were calculated from the discharge curve (eqn (S2†)) and are presented in Fig. 3(e). Remarkably, the free-standing CNF/RGO/MoO_xN_y aerogel film electrode delivered an outstanding specific capacitance of 680 F g $^{-1}$ in 1.0 M H_2SO_4 aqueous electrolyte in a three-electrode configuration at a current density of 1.0 A g $^{-1}$, which is much higher than that of the CNF/RGO aerogel film electrode (388 F g $^{-1}$), and is among the highest values for other types of carbon/metal oxide-based electrodes.[25,39–42] The enhanced specific capacitance of the CNF/RGO/MoO_xN_y aerogel film electrode was attributed to the synergistic electrochemical effect of the graphene, based on the electric double-layer ion absorption, and the pseudocapacitive MoO_xN_y, based on the fast faradaic redox reaction. Furthermore, the CNF/RGO/MoO_xN_y aerogel film electrode still exhibited a specific capacitance of 421 A g $^{-1}$ when the current density was increased to 15 A g $^{-1}$ (*i.e.*, 62% of the capacitance measured at a current density of 1.0 A g $^{-1}$), indicating that the electrode had a good capacitance retention capability due to the highly open and continuous porous structure of the aerogel film electrode, which facilitated ion diffusion and charge transport.

Electrochemical impedance spectroscopy (EIS) was performed to further understand the electrochemical properties of

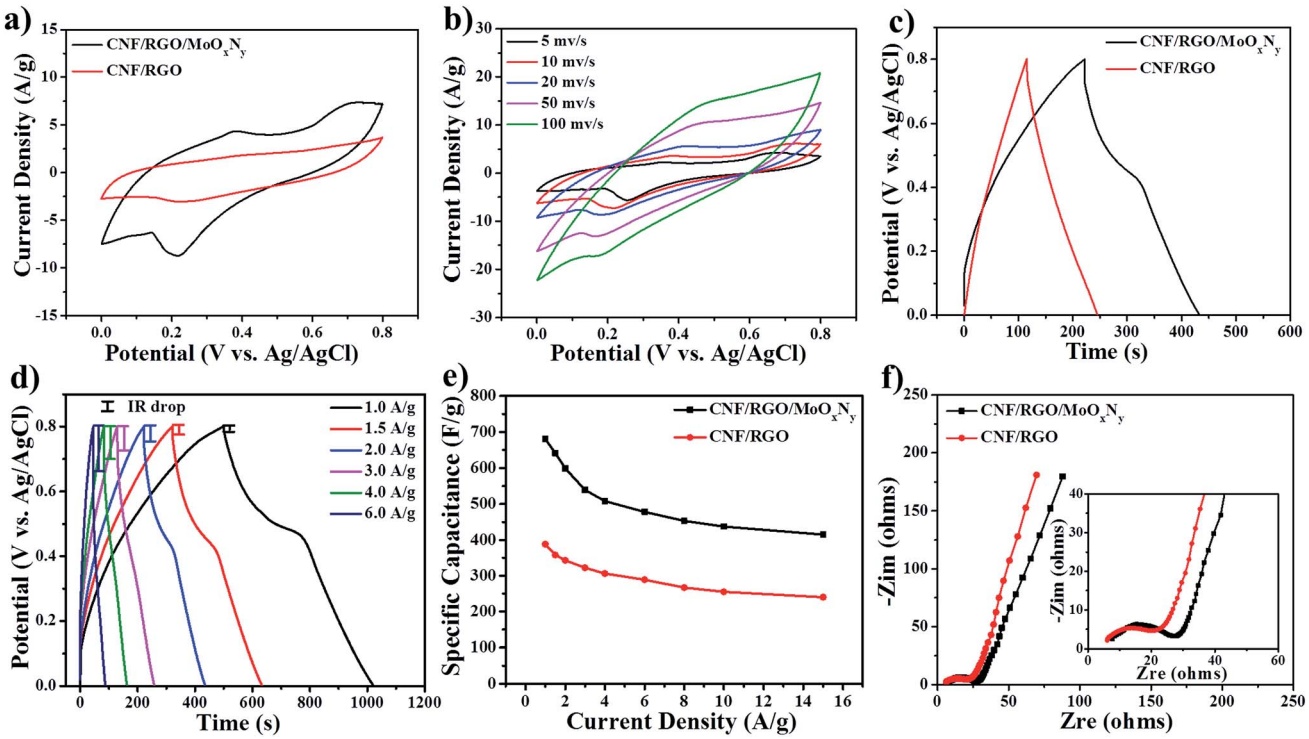

Fig. 3 Electrochemical characterization of the CNF/RGO and CNF/RGO/MoO_xN_y aerogel film electrodes in 1.0 M H_2SO_4 aqueous electrolyte in a three-electrode system. (a) Typical CV curves of the CNF/RGO and CNF/RGO/MoO_xN_y aerogel film electrodes at a scan rate of 10 mV s^{-1}. (b) CV curves of the CNF/RGO/MoO_xN_y aerogel film electrode at different scan rates. (c) Galvanostatic charge–discharge curves of the CNF/RGO and CNF/RGO/MoO_xN_y aerogel film electrodes at a current density of 2.0 A g^{-1}. (d) Galvanostatic charge–discharge curves of the CNF/RGO/MoO_xN_y aerogel film electrodes at different current densities. (e) Specific capacitance of the CNF/RGO and CNF/RGO/MoO_xN_y aerogel film electrodes as a function of current density. (f) Nyquist impedance plots of the CNF/RGO and CNF/RGO/MoO_xN_y aerogel film electrodes with an inset showing the magnified high-frequency region.

the CNF/RGO and CNF/RGO/MoO_xN_y aerogel film electrodes. Fig. 3(f) shows the Nyquist impedance plots of the CNF/RGO and CNF/RGO/MoO_xN_y aerogel film electrodes in the frequency range of 0.01 Hz to 100 kHz, both of which exhibited a semicircle in the high frequency range and a straight line in the low frequency range. The equivalent series resistance (R_{ESR}) of the CNF/RGO/MoO_xN_y aerogel film electrode was 7.7 Ω, which was close to that of the CNF/RGO aerogel film electrode (6.1 Ω). Both CNF/RGO/MoO_xN_y and CNF/RGO aerogel films exhibited a small semicircle in the high frequency range, indicating a low charge transfer resistance.[43,44] Furthermore, the introduction of molybdenum oxynitride did not affect the ion diffusion process as attested to by the similar slopes of the straight lines in the low frequency range of the Nyquist impedance plots of the CNF/RGO and CNF/RGO/MoO_xN_y aerogel film electrodes.[45] The EIS results confirmed that both CNF/RGO and CNF/RGO/MoO_xN_y aerogel films exhibited low charge transfer resistance and fast ion diffusion, which was attributed to the highly porous microstructure exhibited by the aerogel and the superior wettability of the CNFs.[29,46,47] The porous CNF-based aerogel microstructure likely served as electrolyte nano-reservoirs, thereby providing good diffusion channels for electrolyte ions, and enabling the active materials (*i.e.*, RGO and/or MoO_xN_y) in the electrode to be in direct contact with the electrolyte and thus decreasing the distance of ion diffusion.

Room-temperature ILs, possessing good thermal stability, high ion density, and a wide operating potential window,[26] were also examined as electrolytes for the supercapacitors based on these two types of aerogel film electrodes. Fig. 4 shows the electrochemical characterization of the CNF/RGO and CNF/RGO/MoO_xN_y aerogel film electrodes in a 50 vol% [BMPY][NTf_2] acetonitrile solution in a three-electrode system with a potential window of 2.0 to 1.6 V. The CNF/RGO/MoO_xN_y aerogel film electrode exhibited a larger CV area than the CNF/RGO aerogel film electrode (Fig. 4(a)), similar to what was observed for the H_2SO_4 aqueous electrolytes. Furthermore, both CNF/RGO and CNF/RGO/MoO_xN_y aerogel film electrodes showed an increasing enveloped area with increasing scan rate due to the fast charge transfer (Fig. 4(b) and S14(a)†). As shown in Fig. 4(c), the CNF/RGO/MoO_xN_y aerogel film electrode exhibited a longer discharge time, corresponding to a higher capacitance, than CNF/RGO aerogel film electrodes (616 s *vs.* 430 s) at a current density of 2 A g^{-1}. Fig. 4(d) and S14(b)† show the galvanostatic charge–discharge curves of the CNF/RGO and CNF/RGO/MoO_xN_y aerogel film electrodes at various current densities. As shown in Fig. 4(e), the free-standing CNF/RGO/MoO_xN_y aerogel film electrode delivered an outstanding specific capacitance of 518 F g^{-1} in a 50 vol% [BMPY][NTf_2] acetonitrile electrolyte solution in a three-electrode configuration at a current density of 1.0 A

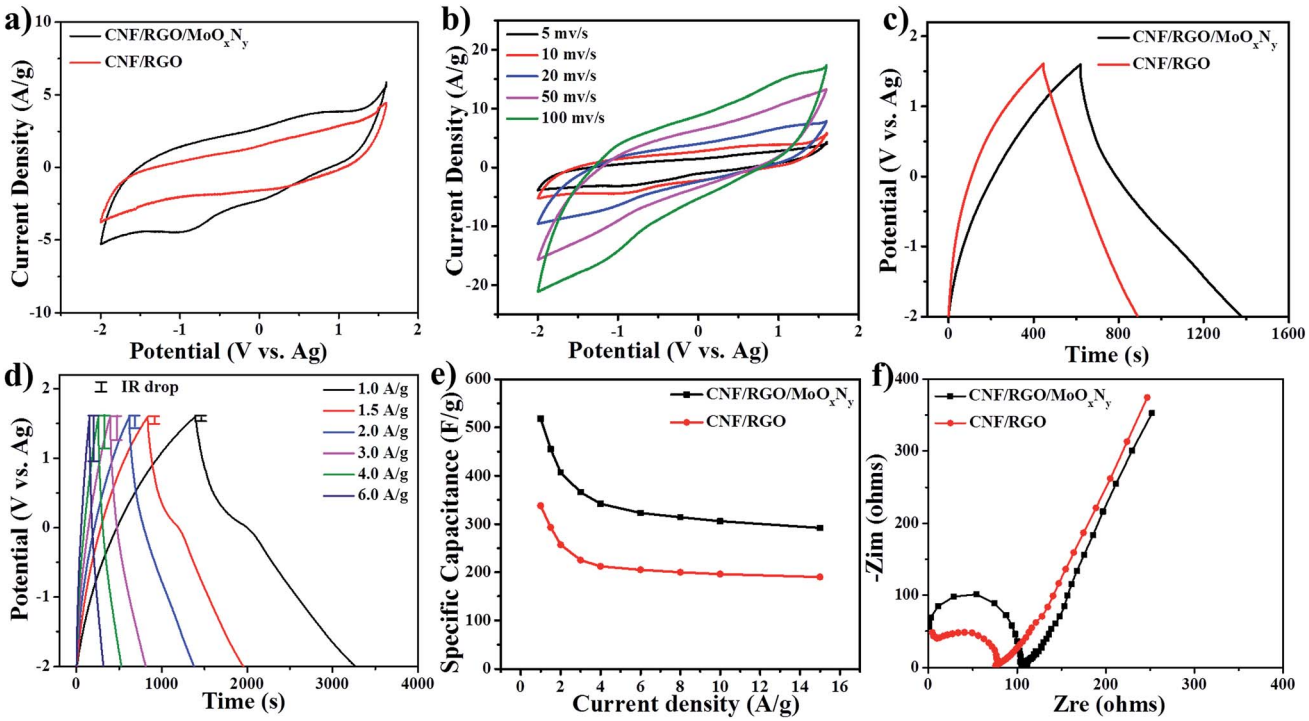

Fig. 4 Electrochemical characterization of the CNF/RGO and CNF/RGO/MoO_xN_y aerogel film electrodes in 50 vol% [BMPY][NTf_2] acetonitrile solution in a three-electrode system. (a) Typical CV curves of the CNF/RGO and CNF/RGO/MoO_xN_y aerogel film electrodes at a scan rate of 10 mV s^{-1}. (b) CV curves of the CNF/RGO/MoO_xN_y aerogel film electrode at different scan rates. (c) Galvanostatic charge–discharge curves of the CNF/RGO and CNF/RGO/MoO_xN_y aerogel film electrodes at a current density of 2.0 A g^{-1}. (d) Galvanostatic charge–discharge curves of the CNF/RGO/MoO_xN_y aerogel film electrodes at different current densities. (e) Specific capacitance of the CNF/RGO and CNF/RGO/MoO_xN_y aerogel film electrodes as a function of current density. (f) Nyquist impedance plots of the CNF/RGO and CNF/RGO/MoO_xN_y aerogel film electrodes.

g $^{-1}$, which again was much higher than that of the CNF/RGO aerogel film electrode (335 F g $^{-1}$), owing to the fast faradaic redox reaction of MoO_xN_y. It is worth mentioning that, even though the specific capacitance of the CNF/RGO/MoO_xN_y aerogel film electrode in 50 vol% [BMPY][NTf_2] acetonitrile electrolyte solution was slightly less than that in the 1.0 M H_2SO_4 aqueous electrolyte, the capacitance was still significantly higher than those reported in other studies with an IL electrolyte.[48–51] This phenomenon was attributed to the highly open and continuous porous structure of the aerogel film electrode that facilitated ion diffusion and charge transport, as well as the aggregation of the graphene was effectively prevented by CNFs and also MoO_xN_y nanobelts. Furthermore, the CNF/RGO/MoO_xN_y aerogel film electrode still retained 56% of the capacitance measured at 1 A g $^{-1}$ when the current density was increased to 15 A g $^{-1}$ (292 F g $^{-1}$). Fig. 4(f) shows the Nyquist impedance plots of the CNF/RGO and CNF/RGO/MoO_xN_y aerogel film electrodes in the frequency range of 0.01 Hz to 100 kHz. The CNF/RGO and CNF/RGO/MoO_xN_y aerogel film electrodes exhibited a similar slope in the low frequency range; however, the CNF/RGO/MoO_xN_y aerogel film electrode showed a larger diameter than the CNF/RGO aerogel film in the high frequency range, which may be ascribed to the slightly slower redox reaction of MoO_xN_y NBs in the IL electrolyte that increased the charge transfer resistance.[39]

3.3. Electrochemical performance of highly flexible and all-solid-state supercapacitors

To further explore the advantages of CNF/RGO/MoO_xN_y aerogel films in flexible and wearable electronic devices, the CNF/RGO/MoO_xN_y aerogel film was used to fabricate all-solid-state-flexible symmetric supercapacitors using polyethylene terephthalate (PET) as a thin flexible substrate and PVA–H_2SO_4 hydrogel or PVDF–P407–[BMPY][NTf_2] ionogel as the electrolyte and separator (Fig. 5(a)). The use of gel electrolytes can reduce the thickness and weight of the supercapacitor, avoid harmful leakage of liquid electrolytes, and simplify the fabrication process since it does not require any special packaging. The all-solid-state supercapacitors are highly flexible and can be easily bent (Fig. 5(b)), which accounts for the excellent mechanical properties and flexibility of the aerogel films.

Similar to what were observed with supercapacitors employing liquid electrolytes, all-solid-state supercapacitors using the CNF/RGO/MoO_xN_y aerogel films as electrodes showed a much higher capacitance than those using the CNF/RGO aerogel films as electrodes, as demonstrated by a larger CV enveloped area (Fig. 5(c)) and a longer discharge time (Fig. 5(e)). Fig. 5(d) presents the CV curves of the CNF/RGO/MoO_xN_y aerogel film-based all-solid-state supercapacitors at scan rates ranging from 5 to 100 mV s^{-1}, of which all exhibited a similar shape without apparent distortion even when the scan rate was

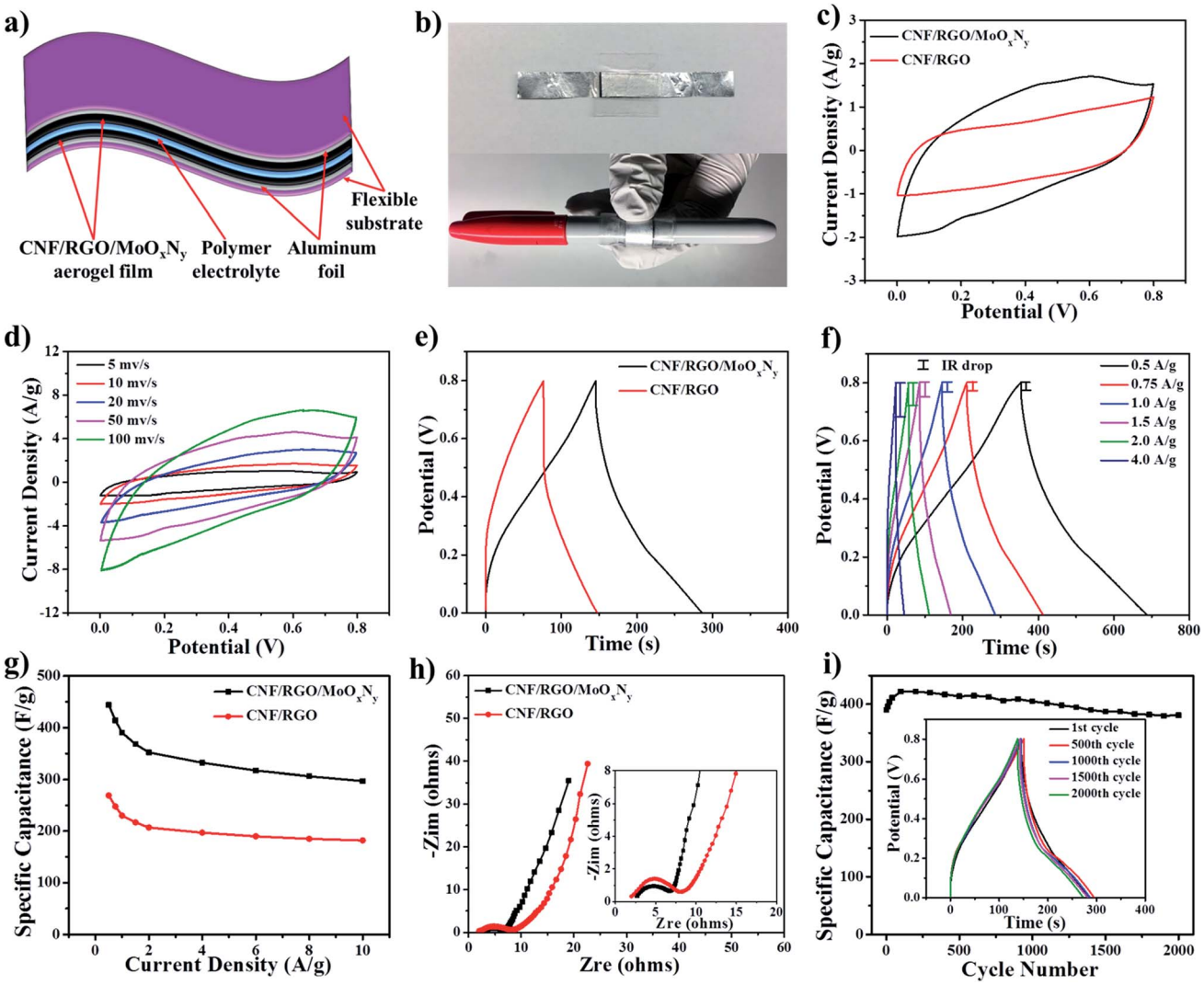

Fig. 5 (a) A schematic diagram of the all-solid-state supercapacitors where the polymer gel electrolyte serves as the electrolyte as well as the separator. (b) A digital graph showing the flexibility of the device. (c–i) Electrochemical characterization of all-solid-state supercapacitors employing PVA–H_2SO_4 hydrogel as the electrolyte: (c) typical CV curves of the CNF/RGO- and CNF/RGO/MoO_xN_y-based solid-state supercapacitors at a scan rate of 10 mV s^{-1}. (d) CV curves of the CNF/RGO/MoO_xN_y-based solid-state supercapacitors at different scan rates. (e) Galvanostatic charge–discharge curves of the CNF/RGO- and CNF/RGO/MoO_xN_y-based solid-state supercapacitors at a current density of 1.0 A g^{-1}. (f) Galvanostatic charge–discharge curves of the CNF/RGO/MoO_xN_y-based solid-state supercapacitors at different current densities. (g) Specific capacitance of the CNF/RGO and CNF/RGO/MoO_xN_y aerogel film electrodes as a function of current density. (h) Nyquist impedance plots of the CNF/RGO- and CNF/RGO/MoO_xN_y-based solid-state supercapacitors. (i) Cycling stability of a solid-state device over 2000 cycles at a current density of 1 A g^{-1}. The inset shows the galvanostatic charge–discharge curves for the 1st, 500th, 1000th, 1500th, and 2000th cycles.

increased to 100 mV s^{-1}, implying fast ion transport and charge transfer in the PVA–H_2SO_4 hydrogel electrolyte. Fig. 5(f) and S16(b)† show nearly triangular and symmetrical shapes of charge–discharge curves of the CNF/RGO and CNF/RGO/MoO_xN_y aerogel film-based all-solid-state supercapacitors at various current densities, indicating excellent capacitive behavior of the solid-state supercapacitors. The specific capacitances at various current densities were calculated from the discharge curve (eqn (S3†)) and are presented in Fig. 5(g). Remarkably, the specific capacitance of the CNF/RGO/MoO_xN_y aerogel film-based all-solid-state supercapacitor was calculated to be 444 F g^{-1} at a current density of 0.5 A g^{-1}, which is among the highest values reported for other types of solid-state supercapacitors.[25,29,30,39] In addition, the solid-state supercapacitor also exhibited an excellent volumetric capacitance of 73.4 F cm^{-3} (eqn (S5†)), and an extremely high areal capacitance of 1110 mF cm^{-2} (eqn (S4†)). When the current density was increased to 10 A g^{-1}, the CNF/RGO/MoO_xN_y aerogel film-based all-solid-state supercapacitor still maintained 68% of the specific capacitance measured at 0.5 A g^{-1} (*i.e.*, 300 *vs.* 444 F g^{-1}).

Both CNF/RGO and CNF/RGO/MoO_xN_y aerogel film-based all-solid-state supercapacitors exhibited a semicircle in the high frequency range and a straight line in the low frequency range in the Nyquist impedance plots (Fig. 5(h)). In particular, both supercapacitors showed a very low R_{ESR} of 2.5 Ω; nevertheless,

the CNF/RGO/MoO_xN_y aerogel film-based all-solid-state supercapacitor exhibited a slightly lower charge transfer resistance, which may be attributable to the excellent mechanical properties of the MoO_xN_y NBs that can maintain the porous structure in the PVA–H_2SO_4 hydrogel electrolyte. The electrochemical cycling stability, which is a very important property for the practical application of all-solid-state supercapacitors, was evaluated by galvanostatic charge–discharge for 2000 cycles at a current density of 1 A g^{-1}. As shown in Fig. 5(i), the specific capacitance increased from 390 to 422 F g^{-1} after the first 200 cycles, which may be attributable to the improved ion accessibility in the porous CNF/RGO/MoO_xN_y aerogel film after repetitive charge–discharge cycles.[39] Thereafter, the specific capacitance underwent a very minor decrease and still retained a capacitance of 381 F g^{-1} after 2000 cycles (98% capacitance retention).

Unfortunately, many practical applications of these solid-state supercapacitors employing a hydrogel electrolyte were limited by their narrow operating potential range (generally less than 1 V). Thus, after optimizing the formulation, an ionogel electrolyte containing 92 wt% [BMPY][NTf_2], 4 wt% PVDF, and 4 wt% P407 was developed and used to fabricate ionogel-based solid-state supercapacitors. Fig. 6 shows various electrochemical characterizations for these ionogel-based solid-state supercapacitor devices in a potential window of 0 to 3.6 V. Both CNF/RGO and CNF/RGO/MoO_xN_y aerogel film-based all-solid-state supercapacitors exhibited excellent capacitive behaviors with very rapid current responses in CV curves (Fig. 6(b) and S18(a)†) and low *IR* (*I*: current, *R*: resistance) drops in charge–discharge curves (Fig. 6(d) and S18(b)†). Furthermore, the CNF/RGO/MoO_xN_y aerogel film-based all-solid-state supercapacitors exhibited higher capacitance than CNF/RGO at various measured current densities. For instance, at a current density of 0.5 A g^{-1}, the specific capacitances for CNF/RGO and CNF/RGO/MoO_xN_y aerogel film-based all-solid-state supercapacitors were 157 and 262 F g^{-1}, respectively. In addition, when the current density was increased to 10 A g^{-1}, the CNF/RGO/MoO_xN_y aerogel film-based all-solid-state supercapacitor still retained a specific capacitance of 163 F g^{-1} (62.2% capacitance retention). Fig. 6(f) showed the Nyquist impedance plots for the CNF/RGO and CNF/RGO/MoO_xN_y aerogel film-based all-solid-state supercapacitors employing PVDF–P407–[BMPY][NTf_2] ionogel as the electrolyte. From this we can see both supercapacitors showed a very low R_{ESR}, while the CNF/RGO/MoO_xN_y aerogel film-based all-solid-state supercapacitor exhibited a slightly higher charge transfer resistance than the CNF/RGO. As shown in Fig. 7(a), the electrochemical stability of the CNF/RGO/MoO_xN_y aerogel film-based all-solid-state supercapacitor employing PVDF–P407–[BMPY][NTf_2] ionogel as the electrolyte was also investigated by a charge–discharge test for 2000 cycles

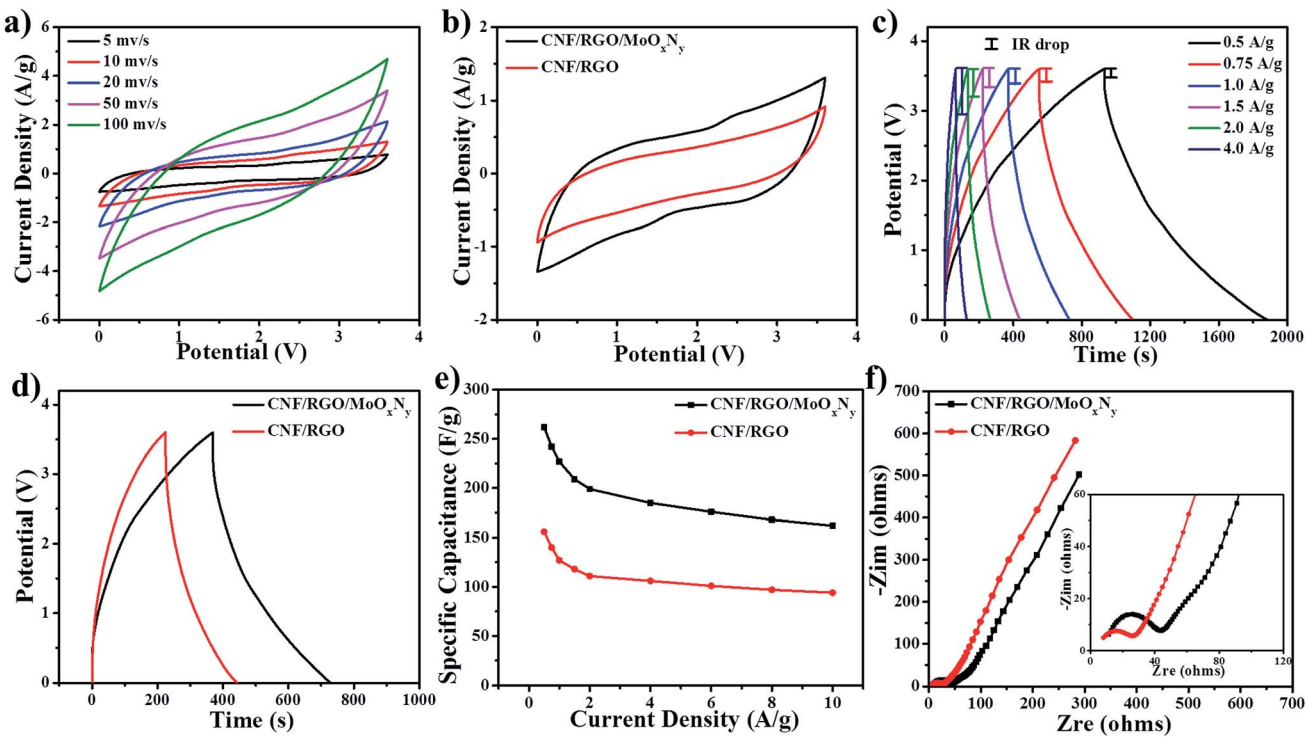

Fig. 6 Electrochemical characterization of the all-solid-state supercapacitors employing PVDF–P407–[BMPY][NTf_2] ionogel as the electrolyte: (a) typical CV curves of the CNF/RGO- and CNF/RGO/MoO_xN_y-based solid-state supercapacitors at a scan rate of 10 mV s^{-1}. (b) CV curves of the CNF/RGO/MoO_xN_y-based solid-state supercapacitors at different scan rates. (c) Galvanostatic charge–discharge curves of the CNF/RGO- and CNF/RGO/MoO_xN_y-based solid-state supercapacitors at a current density of 1.0 A g^{-1}. (d) Galvanostatic charge–discharge curves of the CNF/RGO/MoO_xN_y-based solid-state supercapacitors at different current densities. (e) Specific capacitance of the CNF/RGO and CNF/RGO/MoO_xN_y aerogel film electrodes as a function of current density. (f) Nyquist impedance plots of the CNF/RGO- and CNF/RGO/MoO_xN_y-based solid-state supercapacitors.

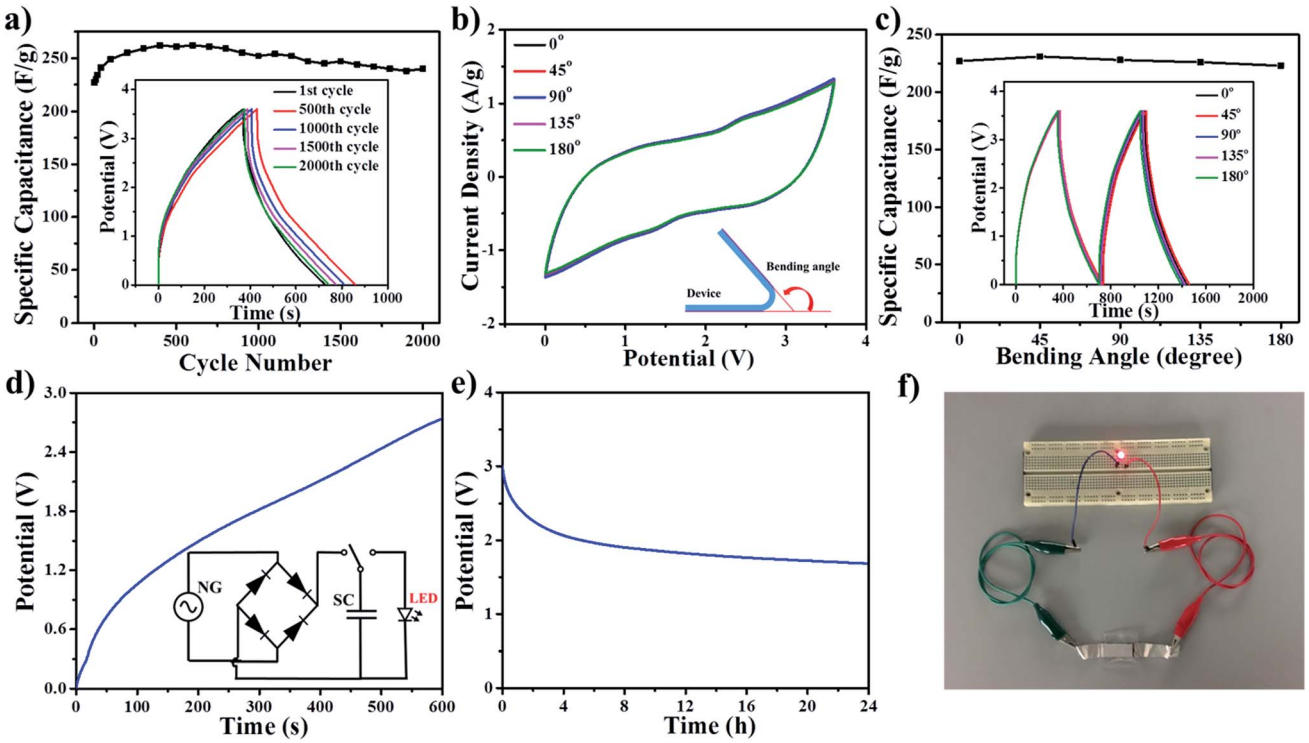

Fig. 7 Characterization of the all-solid-state supercapacitors employing PVDF–P407–[BMPY][NTf$_2$] ionogel as the electrolyte: (a) cycling stability of a solid-state supercapacitor over 2000 cycles at a current density of 1 A g^{-1}. The inset shows the galvanostatic charge–discharge curves for the 1st, 500th, 1000th, 1500th, and 2000th cycles. (b) Cyclic voltammetry curves of a supercapacitor at different bending angles with a scan rate of 10 mV s^{-1}. (c) Dependence of specific capacitance for a supercapacitor at different bending angles. The inset is the charge–discharge curves of a supercapacitor at different bending angles with a current density of 1 A g^{-1}. (d) A solid-state supercapacitor can be easily charged by a porous CNF/PDMS aerogel film-based nanogenerator (NG) under a compressive stress of 0.04 MPa at a frequency of 20 Hz. (e) Self-discharge curves of a solid-state supercapacitor after being charged at 3.0 V for 10 min. (f) A digital picture showing that one single solid-state supercapacitor device can light a red LED well.

at a current density of 1.0 A g^{-1}. The specific capacitance increased from 227 to 262 F g^{-1} after the first 400 cycles, which may be attributable to the improved ion accessibility in the porous CNF/RGO/MoO$_x$N$_y$ aerogel film after repetitive charge–discharge cycles, as reported previously.[39] The specific capacitance then started to decrease slowly thereafter, but it still retained a specific capacitance of 240 F g^{-1} after 2000 cycles (106% capacitance retention). This finding suggests that the supercapacitor made from the CNF/RGO/MoO$_x$N$_y$ aerogel film had superior cycling stability, which may be attributed to the interpenetrating structure formed between the porous aerogel electrodes and the PVDF–P407–[BMPY][NTf$_2$] ionogel electrolyte.[29,52] The SEM images show that the CNF/RGO/MoO$_x$N$_y$ electrode was infiltrated with the electrolyte, and no apparent microstructure change was observed after 2000 charge–discharge cycles (Fig. S20†). Flexibility, which is another important parameter for future energy storage devices that allows for the device to be easily rolled-up, was examined by a bending test. As shown in Fig. S21(a)† and 7(b), bending had almost no effect on the CV curves of the CNF/RGO/MoO$_x$N$_y$ aerogel film-based all-solid-state supercapacitor employing either the PVA–H$_2$SO$_4$ hydrogel or PVDF–P407–[BMPY][NTf$_2$] ionogel as the electrolyte; hence, it could be bent arbitrarily without degrading performance. In addition, the values of specific capacitances remained almost unchanged when the bending angle was increased from 0 to 180 at a current density of 1 A g^{-1} (Fig. S21(b)† and 7(c)), demonstrating that these solid-state supercapacitors were highly flexible and completely recoverable.

Our group previously developed a porous CNF/PDMS aerogel film-based nanogenerator (NG).[53] As shown in Fig. S22,† the porous CNF/PDMS aerogel film-based NG can generate an open-circuit voltage (V_{oc}) of 40.1 V and a short-circuit current (I_{sc}) of 8.2 μA under a compressive stress of 0.04 MPa. The NG was used to charge the CNF/RGO/MoO$_x$N$_y$ aerogel film-based all-solid-state supercapacitor employing PVDF–P407–[BMPY][NTf$_2$] ionogel as the electrolyte through a bridge rectifier. As shown in Fig. 7(d) and ESI video S1,† the supercapacitor could be easily charged up to 2.6 V within 10 min, and the NG-charged solid-state supercapacitor can easily light up an LED.

Self-discharge is one of the great concerns for practical applications. Fig. 7(e) shows the self-discharge curve of a CNF/RGO/MoO$_x$N$_y$ aerogel film-based all-solid-state supercapacitor employing PVDF–P407–[BMPY][NTf$_2$] ionogel as the electrolyte after being charged at 3.0 V for 10 min. The supercapacitor underwent a rapid self-discharge in the first two hours. Thereafter, it exhibited a near plateau region where the potential decreased very slowly. In particular, the supercapacitor still

maintained an output voltage of 1.70 V after 24 h. As a demonstration, a highly flexible and all-solid-state supercapacitor was charged at a constant potential of 3.0 V for 10 min and then used to light up a red LED with a minimum operating potential of 1.65 V. As shown in Fig. 7(f) and ESI video S2,† one single supercapacitor device can light the LED very well for about four hours. It is worth mentioning here that previously reported supercapacitors can light up an LED as well; however, they generally require connecting several supercapacitor devices in series in order to light up one LED.[29,30,39]

To further demonstrate the superior performance of the CNF/RGO/MoO_xN_y aerogel film-based all-solid-state supercapacitors, we calculated the energy and power densities of the supercapacitors employing either hydrogel or ionogel as the electrolyte according to (eqn (S10) and (S11)).† As summarized in a Ragone plot based on the mass (Fig. 8(a)), the CNF/RGO/MoO_xN_y aerogel film-based all-solid-state supercapacitor employing PVA–H_2SO_4 hydrogel as the electrolyte exhibited much higher energy density (*i.e.*, 9.2 W h kg $^{-1}$) compared to carbon cloth[54] or RGO/PEDOT/PSS[55]-based solid state supercapacitors employing hydrogel as the electrolyte. Furthermore, by employing PVDF–P407–[BMPY][NTf_2] ionogel as the electrolyte, the CNF/RGO/MoO_xN_y aerogel film-based all-solid-state supercapacitor showed an energy density of 114.0 W h kg $^{-1}$ at a power density of 442 W kg $^{-1}$ and maintained 38.4 W h kg $^{-1}$ at a power density of 13 900 W kg $^{-1}$. The obtained energy density was among the highest values achieved for any type of state-of-the-art solid-state supercapacitor[54–59] and was even comparable to the energy densities of Li-ion batteries.[6] However, the power density of Li-ion batteries is more than an order of magnitude lower than that of the CNF/RGO/MoO_xN_y aerogel film-based all-solid-state supercapacitor.[6]

For easy comparison, we also calculated the volumetric energy and power densities and presented them in Fig. 8(b), where the data from a high-energy lithium thin-film battery (4 V/500 μA h) and a high-power aluminum electrolytic capacitor (3 V/300 μF) were also included.[44] The CNF/RGO/MoO_xN_y aerogel film-based all-solid-state supercapacitor employing PVDF–P407–[BMPY] [NTf_2] ionogel as the electrolyte exhibited a volumetric energy density up to 18.8 W h L $^{-1}$—a value that is approximately two times higher than that of high-energy lithium thin-film batteries, more than 30 times higher than that of laser-scribed graphene ionogel sandwiched solid-state supercapacitors,[60] and several orders of magnitude higher than that of solid-state supercapacitors employing hydrogel as the electrolyte.[3,60–62] Although the aluminum electrolytic capacitor (3 V/300 μF) can deliver ultra-high power density, it has an energy density that is four orders of magnitude lower than that of CNF/RGO/MoO_xN_y aerogel film-based all-solid-state supercapacitors employing PVDF–P407–[BMPY][NTf_2] ionogel as the electrolyte.

The outstanding electrochemical performance exhibited by the supercapacitors employing the CNF/RGO/MoO_xN_y aerogel film electrodes was attributed to several factors: (1) the partial

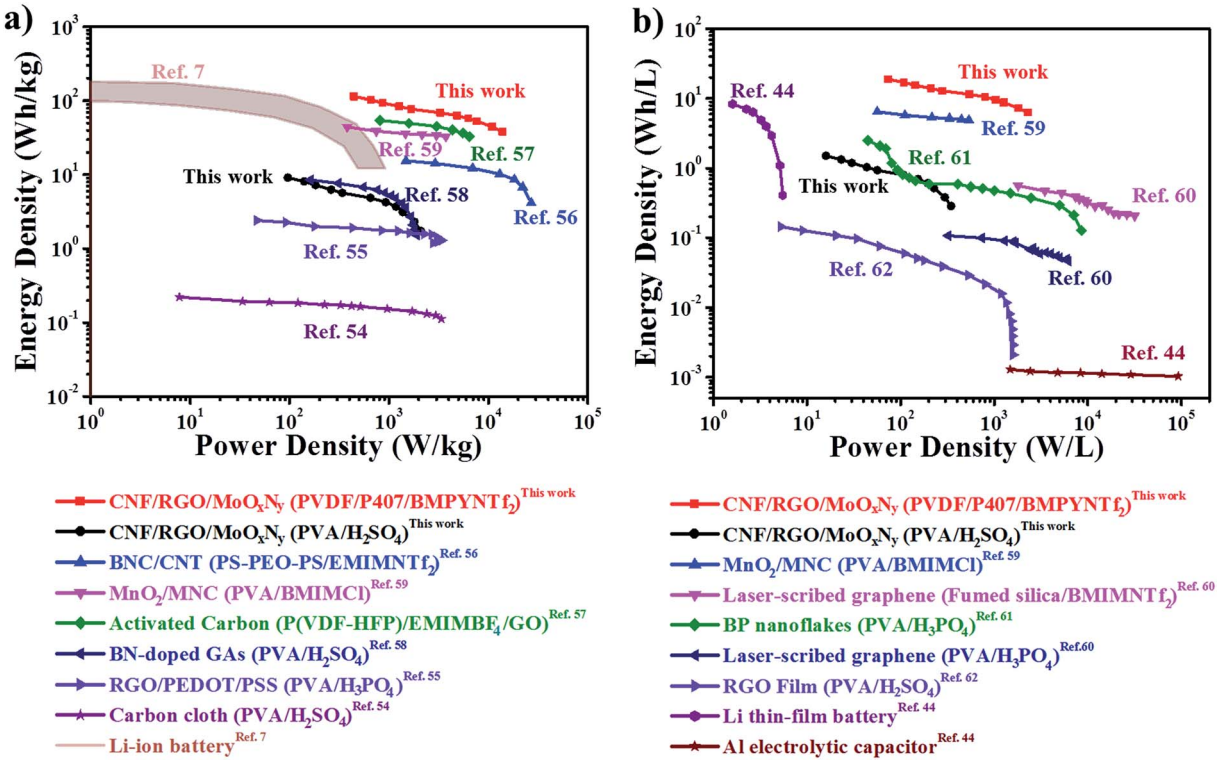

Fig. 8 Ragone plot (a) per mass and (b) per volume of the all-solid-state supercapacitors employing PVA–H_2SO_4 hydrogel or PVDF-P407–[BMPY][NTf_2] ionogel as the electrolyte, compared with several commercial energy storage systems as well as supercapacitors previously reported. BNC: bacterial nanocellulose. MNC: macro/mesoporous Ni/C electrode. GA: graphene aerogel. BP: black phosphorous. P(VDF-HFP): poly(vinylidene fluoride-co-hexafluoropropylene).

reduction and nitrogen doping of MoO_3 nanobelts, which greatly increase the electrical conductivity and electrochemical stability of the resulting CNF/RGO/MoO_xN_y aerogel film electrodes, (2) the aggregation of graphene was effectively prevented by CNFs and also MoO_xN_y nanobelts, (3) the synergistic electrochemical effect of graphene, based on electric double-layer ion absorption, and pseudocapacitive MoO_xN_y, based on fast faradaic redox reactions, and (4) the highly open and continuous porous structure of the aerogel film electrode that facilitated ion diffusion and charge transport.

4. Conclusions

In summary, a free-standing, lightweight, highly porous, and highly flexible CNF/RGO/MoO_xN_y aerogel film electrode was synthesized by freeze-drying a CNF/GO/MoO_3 aqueous dispersion followed by subsequent *in situ* hydrazine reduction. The partial reduction and nitrogen doping of the MoO_3 nanobelts were demonstrated to occur simultaneously with the reduction of GO at a moderate temperature. Supercapacitors made with the CNF/RGO/MoO_xN_y aerogel film electrodes exhibit outstanding specific capacitances and remarkable energy densities in different electrolytes while maintaining high power densities and excellent cycling stability. In particular, the CNF/RGO/MoO_xN_y aerogel film-based highly flexible and all-solid-state supercapacitors using ionogel as the electrolyte demonstrated an energy density of 114 W h kg $^{-1}$ (corresponding to a volumetric energy density of 18.8 W h L $^{-1}$), which is among the highest values achieved for any type of solid-state supercapacitor and is even comparable to the energy densities of Li-ion batteries. Therefore, this study provides a simple, and cost-efficient method for fabricating high-performance porous flexible electrodes *via* a moderate nitrogen doping approach and environmentally friendly freeze-drying process, which can be generalized for the design and fabrication of next-generation flexible energy storage devices with ultra-high energy densities and superior cycling stabilities.

Acknowledgements

The authors gratefully acknowledge the financial support from the University of Wisconsin–Madison. The authors are also thankful to Dr Robert McClain, who is the analytical lab director in the Department of Chemistry, for providing assistance with the electrochemical measurements.

References

1 C. Liu, F. Li, L.-P. Ma and H.-M. Cheng, *Adv. Mater.*, 2010, **22**, E28–E62.
2 H. Nishide and K. Oyaizu, *Science*, 2008, **319**, 737–738.
3 W. Liu, M.-S. Song, B. Kong and Y. Cui, *Adv. Mater.*, 2017, **29**, 1603436.
4 G. Wang, L. Zhang and J. Zhang, *Chem. Soc. Rev.*, 2012, **41**, 797–828.
5 J. M. Tarascon and M. Armand, *Nature*, 2001, **414**, 359–367.
6 P. Simon and Y. Gogotsi, *Nat. Mater.*, 2008, **7**, 845–854.
7 J. Yan, Q. Wang, T. Wei and Z. Fan, *Adv. Energy Mater.*, 2014, **4**, 1300816.
8 X. Xiao, T. Ding, L. Yuan, Y. Shen, Q. Zhong, X. Zhang, Y. Cao, B. Hu, T. Zhai, L. Gong, J. Chen, Y. Tong, J. Zhou and Z. L. Wang, *Adv. Energy Mater.*, 2012, **2**, 1328–1332.
9 L. L. Zhang and X. S. Zhao, *Chem. Soc. Rev.*, 2009, **38**, 2520–2531.
10 L. L. Zhang, R. Zhou and X. S. Zhao, *J. Mater. Chem.*, 2010, **20**, 5983–5992.
11 S. Han, D. Wu, S. Li, F. Zhang and X. Feng, *Adv. Mater.*, 2014, **26**, 849–864.
12 L. Jiang and Z. Fan, *Nanoscale*, 2014, **6**, 1922–1945.
13 Y. Zhang, L. Zhang and C. Zhou, *Acc. Chem. Res.*, 2013, **46**, 2329–2339.
14 S. J. Chae, F. Güneş, K. K. Kim, E. S. Kim, G. H. Han, S. M. Kim, H.-J. Shin, S.-M. Yoon, J.-Y. Choi, M. H. Park, C. W. Yang, D. Pribat and Y. H. Lee, *Adv. Mater.*, 2009, **21**, 2328–2333.
15 Z. Zheng and Q. Gao, *J. Power Sources*, 2011, **196**, 1615–1619.
16 L. Li, X. Zhang, J. Qiu, B. L. Weeks and S. Wang, *Nano Energy*, 2013, **2**, 628–635.
17 T. Kuila, A. K. Mishra, P. Khanra, N. H. Kim and J. H. Lee, *Nanoscale*, 2013, **5**, 52–71.
18 W. Gao, L. B. Alemany, L. Ci and P. M. Ajayan, *Nat. Chem.*, 2009, **1**, 403–408.
19 A. Javadi, Q. Zheng, F. Payen, A. Javadi, Y. Altin, Z. Cai, R. Sabo and S. Gong, *ACS Appl. Mater. Interfaces*, 2013, **5**, 5969–5975.
20 Q. Zheng, Z. Cai and S. Gong, *J. Mater. Chem. A*, 2014, **2**, 3110–3118.
21 X.-J. Wang, R. Nesper, C. Villevieille and P. Novák, *Adv. Energy Mater.*, 2013, **3**, 606–614.
22 T. Brezesinski, J. Wang, S. H. Tolbert and B. Dunn, *Nat. Mater.*, 2010, **9**, 146–151.
23 J. Chang, M. Jin, F. Yao, T. H. Kim, V. T. Le, H. Yue, F. Gunes, B. Li, A. Ghosh, S. Xie and Y. H. Lee, *Adv. Funct. Mater.*, 2013, **23**, 5074–5083.
24 Y. Li, D. Wang, Q. An, B. Ren, Y. Rong and Y. Yao, *J. Mater. Chem. A*, 2016, **4**, 5402–5405.
25 X. Xiao, Z. Peng, C. Chen, C. Zhang, M. Beidaghi, Z. Yang, N. Wu, Y. Huang, L. Miao, Y. Gogotsi and J. Zhou, *Nano Energy*, 2014, **9**, 355–363.
26 M. Galiński, A. Lewandowski and I. Stępniak, *Electrochim. Acta*, 2006, **51**, 5567–5580.
27 A. Lewandowski and A. Świderska-Mocek, *J. Power Sources*, 2009, **194**, 601–609.
28 K. L. Van Aken, M. Beidaghi and Y. Gogotsi, *Angew. Chem., Int. Ed.*, 2015, **54**, 4806–4809.
29 Q. Zheng, Z. Cai, Z. Ma and S. Gong, *ACS Appl. Mater. Interfaces*, 2015, **7**, 3263–3271.
30 B. Yao, L. Huang, J. Zhang, X. Gao, J. Wu, Y. Cheng, X. Xiao, B. Wang, Y. Li and J. Zhou, *Adv. Mater.*, 2016, **28**, 6353–6358.
31 D. C. Marcano, D. V. Kosynkin, J. M. Berlin, A. Sinitskii, Z. Sun, A. Slesarev, L. B. Alemany, W. Lu and J. M. Tour, *ACS Nano*, 2010, **4**, 4806–4814.
32 L. J. Cote, J. Kim, V. C. Tung, J. Y. Luo, F. Kim and J. X. Huang, *Pure Appl. Chem.*, 2011, **83**, 95–110.

33 D. Klemm, F. Kramer, S. Moritz, T. Lindstrom, M. Ankerfors, D. Gray and A. Dorris, *Angew. Chem., Int. Ed.*, 2011, **50**, 5438–5466.
34 R. J. Moon, A. Martini, J. Nairn, J. Simonsen and J. Youngblood, *Chem. Soc. Rev.*, 2011, **40**, 3941–3994.
35 Y. Zhu, S. Murali, W. Cai, X. Li, J. W. Suk, J. R. Potts and R. S. Ruoff, *Adv. Mater.*, 2010, **22**, 3906–3924.
36 S. Li, W. B. Kim and J. S. Lee, *Chem. Mater.*, 1998, **10**, 1853–1862.
37 W. Ji, R. Shen, R. Yang, G. Yu, X. Guo, L. Peng and W. Ding, *J. Mater. Chem. A*, 2014, **2**, 699–704.
38 S. Stankovich, D. A. Dikin, R. D. Piner, K. A. Kohlhaas, A. Kleinhammes, Y. Jia, Y. Wu, S. T. Nguyen and R. S. Ruoff, *Carbon*, 2007, **45**, 1558–1565.
39 K. Zhou, W. Zhou, X. Liu, Y. Sang, S. Ji, W. Li, J. Lu, L. Li, W. Niu, H. Liu and S. Chen, *Nano Energy*, 2015, **12**, 510–520.
40 D. Hanlon, C. Backes, T. M. Higgins, M. Hughes, A. O'Neill, P. King, N. McEvoy, G. S. Duesberg, B. Mendoza Sanchez, H. Pettersson, V. Nicolosi and J. N. Coleman, *Chem. Mater.*, 2014, **26**, 1751–1763.
41 K. Liang, T. Gu, Z. Cao, X. Tang, W. Hu and B. Wei, *Nano Energy*, 2014, **9**, 245–251.
42 G. Yu, L. Hu, N. Liu, H. Wang, M. Vosgueritchian, Y. Yang, Y. Cui and Z. Bao, *Nano Lett.*, 2011, **11**, 4438–4442.
43 Y. Shao, M. F. El-Kady, C.-W. Lin, G. Zhu, K. L. Marsh, J. Y. Hwang, Q. Zhang, Y. Li, H. Wang and R. B. Kaner, *Adv. Mater.*, 2016, **28**, 6719–6726.
44 M. F. El-Kady, V. Strong, S. Dubin and R. B. Kaner, *Science*, 2012, **335**, 1326–1330.
45 J. Li, H. Xie, Y. Li, J. Liu and Z. Li, *J. Power Sources*, 2011, **196**, 10775–10781.
46 Z. Gui, H. Zhu, E. Gillette, X. Han, G. W. Rubloff, L. Hu and S. B. Lee, *ACS Nano*, 2013, **7**, 6037–6046.
47 K. Gao, Z. Shao, J. Li, X. Wang, X. Peng, W. Wang and F. Wang, *J. Mater. Chem. A*, 2013, **1**, 63–67.
48 C. Peng, Z. Wen, Y. Qin, L. Schmidt-Mende, C. Li, S. Yang, D. Shi and J. Yang, *ChemSusChem*, 2014, **7**, 777–784.
49 M. Shi, S. Kou and X. Yan, *ChemSusChem*, 2014, **7**, 3053–3062.
50 C.-H. Yang, P.-L. Huang, X.-F. Luo, C.-H. Wang, C. Li, Y.-H. Wu and J.-K. Chang, *ChemSusChem*, 2015, **8**, 1779–1786.
51 H. Liu, P. He, Z. Li, Y. Liu and J. Li, *Electrochim. Acta*, 2006, **51**, 1925–1931.
52 S. Li, D. Huang, B. Zhang, X. Xu, M. Wang, G. Yang and Y. Shen, *Adv. Energy Mater.*, 2014, **4**, 1301655.
53 Q. Zheng, H. Zhang, H. Mi, Z. Cai, Z. Ma and S. Gong, *Nano Energy*, 2016, **26**, 504–512.
54 G. Wang, H. Wang, X. Lu, Y. Ling, M. Yu, T. Zhai, Y. Tong and Y. Li, *Adv. Mater.*, 2014, **26**, 2676–2682.
55 Y. Liu, B. Weng, J. M. Razal, Q. Xu, C. Zhao, Y. Hou, S. Seyedin, R. Jalili, G. G. Wallace and J. Chen, *Sci. Rep.*, 2015, **5**, 17045.
56 Y. J. Kang, S.-J. Chun, S.-S. Lee, B.-Y. Kim, J. H. Kim, H. Chung, S.-Y. Lee and W. Kim, *ACS Nano*, 2012, **6**, 6400–6406.
57 X. Yang, F. Zhang, L. Zhang, T. Zhang, Y. Huang and Y. Chen, *Adv. Funct. Mater.*, 2013, **23**, 3353–3360.
58 Z.-S. Wu, A. Winter, L. Chen, Y. Sun, A. Turchanin, X. Feng and K. Müllen, *Adv. Mater.*, 2012, **24**, 5130–5135.
59 J. Zhi, O. Reiser, Y. Wang and A. Hu, *Nanoscale*, 2016, **8**, 11976–11983.
60 M. F. El-Kady and R. B. Kaner, *Nat. Commun.*, 2013, **4**, 1475.
61 C. Hao, B. Yang, F. Wen, J. Xiang, L. Li, W. Wang, Z. Zeng, B. Xu, Z. Zhao, Z. Liu and Y. Tian, *Adv. Mater.*, 2016, **28**, 3194–3201.
62 Z. S. Wu, K. Parvez, X. Feng and K. Müllen, *Nat. Commun.*, 2013, **4**, 2487.

